

# Anomalous Andreev Reflection on a Torus-Shaped Fermi Surface

Wei Luo,<sup>1,2</sup> Wei Chen,<sup>1,3,\*</sup> and D. Y. Xing<sup>1,3</sup>

<sup>1</sup>National Laboratory of Solid State Microstructures and School of Physics, Nanjing University, Nanjing 210093, China

<sup>2</sup>School of Science, Jiangxi University of Science and Technology, Ganzhou 341000, China

<sup>3</sup>Collaborative Innovation Center of Advanced Microstructures, Nanjing University, Nanjing 210093, China

(Dated: January 13, 2022)

Andreev reflection (AR) refers to the electron-hole conversion at the normal metal-superconductor interface. In a three-dimensional metal with spherical Fermi surface, retro (specular) AR can occur with the sign reversal of all three (a single) components of particle velocity. Here, we predict a novel type of AR with the inversion of two velocity components, dubbed “anomalous-trajectory Andreev reflection” (AAR), which can be realized in a class of materials with torus-shaped Fermi surface, such as doped nodal line semimetals. For its toroidal circle perpendicular to the interface, the Fermi torus doubles the AR channels and generates multiple AR processes. In particular, the AAR and retro AR are found to dominate electron transport in the light and heavy doping regimes, respectively. We show that the AAR visibly manifests as a ridge structure in the spatially resolved nonlocal conductance, in contrast to the peak structure for the retro AR. Our work opens a new avenue for the AR spectroscopy and offers a clear transport signature of torus-shaped Fermi surface.

Andreev reflection (AR) describes the electron-hole conversion at the interface between a normal metal and a superconductor, by which a pair of electrons penetrate into the superconductor and form a Cooper pair [1]. It dominates the electron transport within the superconducting gap due to the prohibition of single-particle transmission [2]. AR spectroscopy has become a powerful tool for the detection of various properties of electronic systems, such as the pairing order parameter in unconventional superconductors [3–5], spin polarization of metal [6, 7], Dirac/Weyl fermion with linear dispersion [8–10], and Majorana zero mode in topological superconductors [11, 12]. It may also have potential applications in quantum information processing [13–15] and spintronics [16].

One unique feature of the conventional AR is that the reflected hole retraces the path of the incident electron by inverting all velocity components [1], so-called retro AR (RAR); see Fig. 1(a). Interestingly, if the incident electron and reflected hole are from the conduction and valence band respectively, specular AR (SAR) may occur [8], in which only the velocity component perpendicular to the interface is inverted; see Fig. 1(b). The SAR is hard to achieve in conventional semiconductors, whose energy gap exceeds the superconducting gap so as to block the reflected hole. However, massless Dirac Fermion in various materials, such as graphene and topological semimetals is favorable for the observation of SAR [8, 10, 17]. In two dimensions, the RAR and SAR constitute a complete set of AR. Interestingly, the phenomenon gets enriched in three dimensions due to the additional velocity component.

In this Letter, we predict the third type of AR in which two of three velocity components are inverted, dubbed “anomalous-trajectory Andreev reflection” (AAR); see Fig. 1(d) and Table I for clarity. We show that the AAR can occur in the system with a torus-shaped Fermi

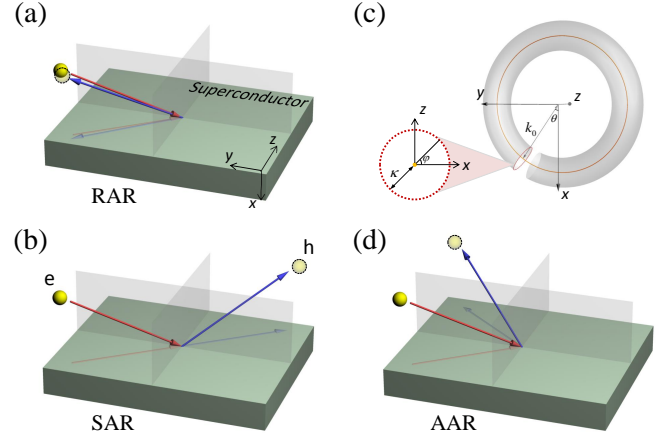


FIG. 1. Schematic illustration of three types of AR, an electron (e) incident from the normal metal is reflected into a hole (h): (a) RAR, (b) SAR, and (d) AAR with three, one and two velocity components reversed relative to the incident electron. The projected trajectories on the  $y$ - $z$  plane are indicated. (c) Torus-shaped Fermi surface of a doped nodal line semimetal with major radius  $k_0$ , minor radius  $\kappa$ , toroidal angle  $\theta$ , and poloidal angle  $\varphi$ .

surface [18–21] as shown in Fig. 1(c), which exists in a large category of materials called nodal line semimetals [18–35]. The Fermi torus differs in topology from the conventional Fermi sphere, which can lead to anomalous transport signatures [36, 37]. Here, we consider a metal-superconductor junction oriented along the  $x$ -direction and the toroidal circle of the Fermi torus is perpendicular to the interface. For lateral momentum ( $k_y, k_z$ ) conserved, there exist two AR channels with different sign in the lateral velocities [cf. Table I]. Specifically, we find that the AAR dominates the inter-band scattering regime in which the electron and reflected hole are from different bands, as the sample is weakly doped such that the chemical potential is much smaller than the superconducting

TABLE I. Comparison of velocity inversion in the RAR, SAR, and AAR.

	$v_x$	$v_y$	$v_z$
RAR	—	—	—
SAR	—	+	+
AAR	—	— (+)	+

gap ( $\mu \ll \Delta$ ). The main feature of AAR is that only one lateral velocity component inverts its sign, indicating an unconventional trajectory of the reflected hole wave packet, that is, extended in one direction while localized in the other. Such a feature can be probed by non-local scanning tunneling spectroscopy (STM), in which the conductance exhibits a spatially resolved ridge structure, thus providing a clear signature of AAR.

We consider a spin-degenerate nodal line semimetal captured by the following Hamiltonian

$$H_{\text{NL}} = \hbar\lambda(k_x^2 + k_y^2 - k_0^2)\sigma_x + \hbar vk_z\sigma_y - \mu, \quad (1)$$

where the Pauli matrices  $\sigma_{x,y}$  operate on the pseudo-spin (orbital/sublattice),  $k_0$  is the radius of the nodal loop defined by the band crossing,  $\lambda$  and  $v$  are model parameters, and  $\mu$  is the chemical potential. In order to study the electron-hole scattering, we work on the Bogoliubov-de Gennes Hamiltonian for the whole junction

$$\begin{aligned} \mathcal{H} &= \mathcal{H}_{\text{NL}}\Theta(-x) + \mathcal{H}_{\text{S}}\Theta(x) + U\delta(x)\tau_z, \\ \mathcal{H}_{\text{NL}} &= H_{\text{NL}} \otimes \tau_z, \quad \mathcal{H}_{\text{S}} = \varepsilon_{\mathbf{k}}\sigma_0 \otimes \tau_z + \Delta\sigma_0 \otimes \tau_x, \end{aligned} \quad (2)$$

where  $\Theta(x)$  is the unit step function and  $\tau_{x,z}$  are Pauli matrices in the Nambu space,  $\mathcal{H}_{\text{NL}}$  and  $\mathcal{H}_{\text{S}}$  correspond to the nodal line semimetal and the conventional  $s$ -wave superconductor, respectively, and  $U\delta(x)\tau_z$  is a  $\delta$ -function interface barrier at  $x = 0$ . The normal state energy  $\varepsilon_{\mathbf{k}} = \hbar^2\mathbf{k}^2/(2m) - \mu_s$  (relative to the chemical potential  $\mu_s$ ) in the superconductor and the pair potential  $\Delta$  are diagonal in the pseudo-spin space, and  $m$  is the effective mass.

For a slightly doped nodal line semimetal, in which  $\mu \ll \hbar\lambda k_0^2$  and the Fermi surface possesses a torus shape, we can linearize and parameterize the Hamiltonian as  $\mathcal{H}_{\text{NL}} \simeq [\hbar v_0\kappa(\cos\varphi\sigma_x + \sin\varphi\sigma_y) - \mu]\otimes\tau_z$  around the nodal loop by substituting  $k_x = (k_0 + \kappa\cos\varphi)\cos\theta$ ,  $k_y = (k_0 + \kappa\cos\varphi)\sin\theta$  and  $k_z = \kappa\sin\varphi/\alpha$ , where  $\alpha = v/v_0$  is the ratio between the velocities in the  $z$  direction and  $v_0 = 2\lambda k_0$  in the  $x$ - $y$  plane. All states are then specified by the minor radius  $\kappa$ , toroidal angle  $\theta$ , and poloidal angle  $\varphi$  of the torus; see Fig. 1(c). The excitation energies for electron and hole are  $E_e = \pm\hbar v_0\kappa - \mu$  and  $E_h = \mp\hbar v_0\kappa + \mu$ , which are independent of  $\theta$  and  $\varphi$ , with “ $\pm$ ” (“ $\mp$ ”) corresponding to the conduction and valence band, respectively.

The Fermi torus has nontrivial effects on AR by doubling the reflection channels. Consider an electron in the conduction band incident on the interface at  $x = 0$  from

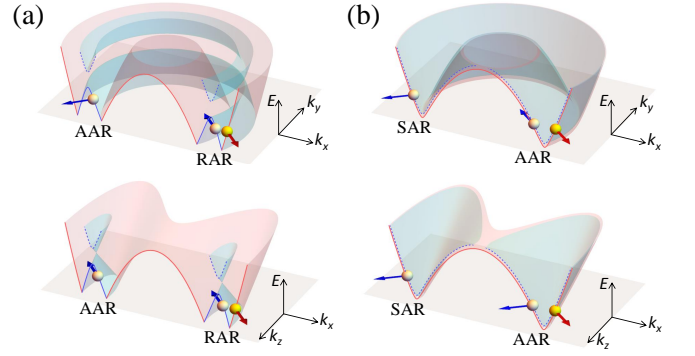


FIG. 2. The dispersion of electron (red band) and hole (blue band) with (a) finite and (b) vanishing chemical potential, in which solid and dashed boundaries denote conduction and valence bands, respectively. For an incident electron (red arrow), there are (a) two intra-band AR channels for the hole (blue arrows): RAR and AAR, and (b) two inter-band AR channels: AAR and SAR.

the normal side, with energy  $E$  and transverse wave vector  $(k_y, k_z)$ , or equivalently labeled by  $(\kappa_e, \theta_e, \varphi_e)$ , with  $\kappa_e = (E + \mu)/(\hbar v_0)$ . There are two possible incident states ( $k_x > 0$  or  $k_x < 0$ ) on the Fermi torus, and we first focus on the case of  $k_x > 0$  or  $\theta_e \in (-\pi/2, \pi/2)$ . The velocity components are given by  $v_x^e = v_0 \cos\varphi_e \cos\theta_e$ ,  $v_y^e = v_0 \cos\varphi_e \sin\theta_e$  and  $v_z^e = v \sin\varphi_e$ . There are two scenarios of AR depending on the relative magnitude of  $E$  and  $\mu$ . (i) For  $E < \mu$ , the Andreev reflected hole is in the conduction band, the same as the incident electron, indicating an intra-band process; see Fig. 2(a). There are two reflecting hole states:  $h_1 : (\kappa_h, \theta_h, \varphi_h)$  and  $h_2 : (\kappa_h, \pi - \theta_h, \pi - \varphi_h)$  where  $\kappa_h = |E - \mu|/(\hbar v_0)$  is the minor radius of the hole torus,  $\theta_h \simeq \theta_e$  up to a small correction of the order  $\kappa_{e(h)}/k_0$ , and  $\sin\varphi_h/\sin\varphi_e = \kappa_e/\kappa_h$ . Since the dispersion of the hole in the conduction band is opposite in sign to that for the electron, the  $h_1$  state inverts all three velocity components, that is RAR. For the  $h_2$  state, different reflection angles contribute additional minus sign to  $v_y^h$ , so that only  $v_x^h$  and  $v_z^h$  are inverted in the end, which is AAR. (ii) For  $E > \mu$ , the Andreev reflected hole is in the valence band, which is an inter-band process. A typical case of  $\mu \simeq 0$  is illustrated in Fig. 2(b). Now the hole possesses the same sign in dispersion as the electron, and two AR states are  $\tilde{h}_1 : (\kappa_h, \pi - \theta_h, \varphi_h)$  and  $\tilde{h}_2 : (\kappa_h, \theta_h, \pi - \varphi_h)$  by requiring  $v_x^h < 0$ . Correspondingly, the hole state  $\tilde{h}_1$  contains only the sign reversal in  $v_x^h$ , being the SAR. Meanwhile, for the state  $\tilde{h}_2$  both  $v_x^h$  and  $v_y^h$  change the sign [cf. Fig. 1(d)], which is again AAR. From the qualitative analysis above, one finds that all types of AR can occur on the Fermi torus, as summarized in Table I.

Next we solve the scattering problem in detail to give quantitative results. For an incident electron  $e_1$  with  $k_x > 0$ , the wave functions on both sides of the junction

are given by

$$\begin{aligned}
\psi &= [\psi_{\text{NL}}\Theta(-x) + \psi_{\text{S}}\Theta(x)]e^{ik_y y + ik_z z}, \\
\psi_{\text{NL}} &= (e^{ik_1^e x} + r_{e_1}^{e_1} e^{-ik_1^e x})|e_1\rangle + r_{e_1}^{e_2} e^{ik_2^e x}|e_2\rangle \\
&\quad + r_{e_1}^{h_1} e^{i\eta k_1^h x}|h_1\rangle + r_{e_1}^{h_2} e^{-i\eta k_2^h x}|h_2\rangle, \\
\psi_{\text{S}} &= (t_1|s_1\rangle + t_2|s_2\rangle)e^{iq_1 x} + (t_3|s_3\rangle + t_4|s_4\rangle)e^{-iq_2 x}.
\end{aligned} \tag{3}$$

Here,  $\psi_{\text{NL}}$  denotes the wave function of the nodal line semimetal for  $x < 0$  and its spinor part is given by  $|e_1\rangle = (1/\sqrt{2}, e^{i\varphi_e}/\sqrt{2}, 0, 0)$ ,  $|e_2\rangle = (1/\sqrt{2}, -e^{-i\varphi_e}/\sqrt{2}, 0, 0)$ ,  $|h_1\rangle = (0, 0, 1/\sqrt{2}, \eta e^{i\varphi_h}/\sqrt{2})$ , and  $|h_2\rangle = (0, 0, 1/\sqrt{2}, -\eta e^{-i\varphi_h}/\sqrt{2})$  with  $\varphi_{e(h)} = \sin^{-1}[\alpha k_z/\kappa_{e(h)}]$  and  $\eta = \text{sgn}(\mu - E)$ . The  $x$  components of the wave vectors are  $k_1^{e(h)} = [k_0 + \kappa_{e(h)} \cos \varphi_{e(h)}] \cos \theta_{e(h)}^+$  and  $k_2^{e(h)} = [k_0 - \kappa_{e(h)} \cos \varphi_{e(h)}] \cos \theta_{e(h)}^-$  with  $\theta_{e(h)}^\pm = \sin^{-1}[k_y/(k_0 \pm \kappa_{e(h)} \cos \varphi_{e(h)})]$ . The amplitudes  $r_{e_1}^{e_1}$  and  $r_{e_1}^{e_2}$  correspond to the normal reflection, and  $r_{e_1}^{h_1}$  and  $r_{e_1}^{h_2}$  are marked as the RAR (SAR) and AAR, respectively.  $\psi_{\text{S}}$  stands for the wave function of the superconductor for  $x > 0$ , in which  $t_1, \dots, t_4$  are the quasiparticle tunneling amplitudes, and the wave vectors are  $q_{1,2} = [2m(\mu_s \pm \sqrt{E^2 - \Delta^2})/\hbar^2 - k_y^2 - k_z^2]^{1/2}$ . The spinor part of  $\psi_{\text{S}}$  is given by  $|s_1\rangle = |s_3\rangle^* = (1/\sqrt{2}, 0, e^{-i\beta}/\sqrt{2}, 0)$  and  $|s_2\rangle = |s_4\rangle^* = (0, 1/\sqrt{2}, 0, e^{-i\beta}/\sqrt{2})$  with  $\beta = \cos^{-1}(E/\Delta)$  for  $E < \Delta$  and  $i \cosh^{-1}(E/\Delta)$  for  $E > \Delta$ . All scattering coefficients can be solved by boundary conditions,  $\psi_{\text{NL}}(0) = \psi_{\text{S}}(0) = \psi(0)$  and  $\lambda \sigma_x \psi'_{\text{NL}}(0) - \frac{\hbar^2}{2m} \sigma_0 \psi'_{\text{S}}(0) = -\sigma_0 U \psi(0)$ .

To see some analytical results, we first consider a transparent interface ( $U = 0$ ) and two limiting cases:  $E, \Delta \ll \mu$  and  $E, \Delta \gg \mu$ , such that we have  $\theta_{e(h)}^\pm \simeq \theta_h^\pm = \theta$  and  $\varphi_e \simeq \varphi_h = \varphi$ . More general numerical results will be given later. For  $E, \Delta \ll \mu$ , the amplitudes  $r_{e_1}^{h_1}$  for the RAR process and  $r_{e_1}^{h_2}$  for the AAR process with inverted  $v_x$  and  $v_z$  are obtained as

$$\begin{aligned}
r_{e_1}^{h_1} &= \frac{2\chi[2\chi \cos \beta \cos^2 \varphi + i \sin \beta (\cos^2 \varphi + \chi^2)]}{[i \sin \beta (\cos^2 \varphi + \chi^2) + 2\chi \cos \beta]^2 - 4\chi^2 \sin^2 \varphi}, \\
r_{e_1}^{h_2} &= \frac{-2\chi e^{i\varphi} \sin \beta \sin \varphi (\cos^2 \varphi - \chi^2)}{[i \sin \beta (\cos^2 \varphi + \chi^2) + 2\chi \cos \beta]^2 - 4\chi^2 \sin^2 \varphi},
\end{aligned} \tag{4}$$

where  $\chi = v_x^e/v_x^F$  with  $v_x^e$  as the  $x$ -direction velocity of electron in the nodal line semimetal and  $v_x^F = \sqrt{2m\mu_s - \hbar^2(k_y^2 + k_z^2)}/m$  as that in the superconductor. In this case, the RAR process dominates the electron transport for  $E < \Delta$ . For  $E = \Delta$  and thus  $\beta = 0$ , we have  $r_{e_1}^{h_1} = 1$  and  $r_{e_1}^{h_2} = 0$ , indicating that perfect RAR can be implemented for all incident angles ( $\theta, \varphi$ ).

For  $E, \Delta \gg \mu$ , the AR amplitudes are reduced to

$$r_{e_1}^{h_1} = 0, \quad r_{e_1}^{h_2} = \frac{2\chi e^{i\varphi} \cos \varphi}{i \sin \beta (\cos^2 \varphi + \chi^2) + 2\chi \cos \beta}, \tag{5}$$

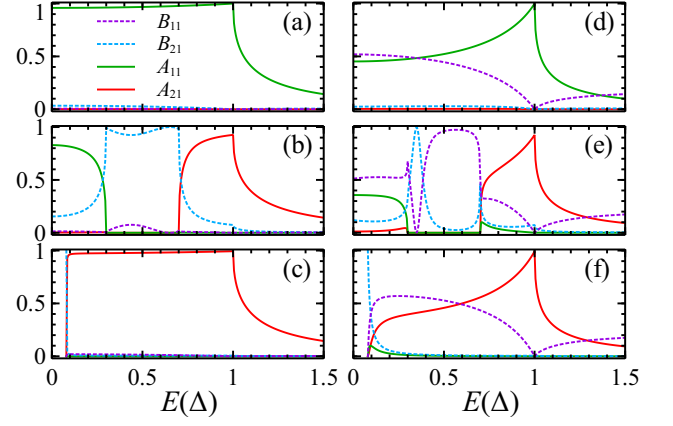


FIG. 3. Probabilities of various AR processes as functions of energy. Specifically,  $A_{21}$  is the AAR probability and  $A_{11}$  corresponds to RAR (SAR) in the intra (inter)-band regime. The interface barrier  $Z = 2U/(\hbar v_0) = 0$  in the left panel and  $Z = 1$  in the right panel. The chemical potential and  $k_z$  are taken as (a,d)  $\mu = 40\Delta$  and  $k_z = 0.2k_0$ , (b,e)  $\mu = 0.5\Delta$  and  $k_z = k_0/200$ , and (c,f)  $\mu = 0$  and  $k_z = k_0/500$ , and  $k_y = 0.5k_0$  is adopted in (a-f). The parameters for the superconductor are  $\Delta = 2$  meV,  $\mu_s = 2$  eV,  $m = 0.1m_e$  and those for the nodal line semimetal are  $k_0 = 2$  nm $^{-1}$ ,  $v_0 = 3 \times 10^5$  m/s,  $\alpha = 0.2$ .

where  $r_{e_1}^{h_1}$  and  $r_{e_1}^{h_2}$  correspond to the SAR and AAR processes, respectively. In this case, one finds that the AAR dominates the electron transport with the inversion of  $v_x$  and  $v_y$ . In particular, the AAR amplitude becomes  $r_{e_1}^{h_2} = e^{i\varphi} \cos \varphi$  at  $E = \Delta$ , solely determined by the poloidal angle  $\varphi$ . The vanishing SAR in Eq. (5) stems from the orthogonality between the pseudo-spin texture of the incident and reflected waves, i.e.,  $\langle h_1 | \tau_x | e_1 \rangle = 0$  for  $\eta = -1$ . However, the existence of an interface barrier can induce multiple scattering and lead to a finite SAR probability [cf. Fig. 3(f)]. For the incident electron  $e_2$  with  $k_x < 0$ , the similar calculations for wave functions can be done, and the corresponding AR amplitudes of  $e_1$  ( $k_x > 0$ ) and  $e_2$  ( $k_x < 0$ ) are shown to be related by  $r_{e_2}^{h_1}(\varphi) = r_{e_1}^{h_2}(-\varphi)$  and  $r_{e_2}^{h_2}(\varphi) = r_{e_1}^{h_1}(-\varphi)$ , where  $r_{e_2}^{h_1}$  is the AAR amplitude of the  $e_2$  electron, and  $r_{e_2}^{h_2}$  corresponds to its RAR or SAR amplitude.

For more general cases, we plot the numerical results of various reflection probabilities in Fig. 3, which are defined as  $B_{11} = |r_{e_1}^{e_1}|^2$ ,  $B_{21} = |r_{e_1}^{e_2}|^2 v_{2x}^e/v_{1x}^e$ ,  $A_{11} = |r_{e_1}^{h_1}|^2 v_{1x}^h/v_{1x}^e$ , and  $A_{21} = |r_{e_1}^{h_2}|^2 v_{2x}^h/v_{1x}^e$  with the ratio between the velocities of reflected and incident waves involved. In Figs. 3(a) and (c), the calculated results recover the conclusions drawn from Eqs. (4) and (5) in two limiting cases. Between the two, as shown in Fig. 3(b), there is a crossover from the intra-band RAR-dominated process to inter-band AAR-dominated one [38]. The effect of the interface barrier is considered in Figs. 3(d)-(f), which enhances the normal electron reflection, but does not much change the relative strength of various AR pro-

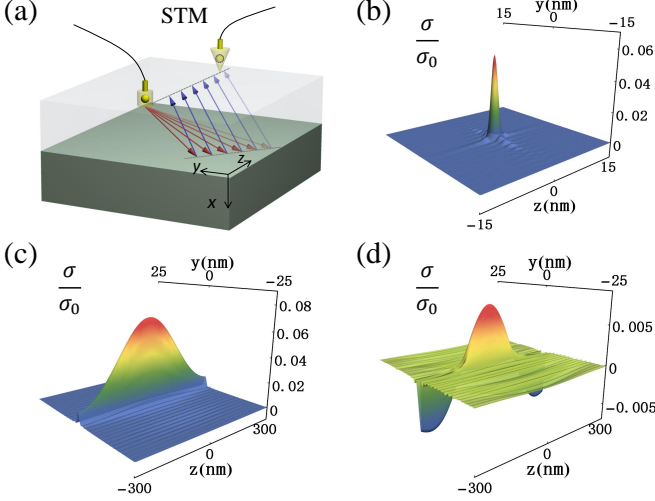


FIG. 4. (a) Sketch of the two-terminal setup for nonlocal conductance measurement. (b) Nonlocal conductance in the RAR regime with  $eV = 0$  and  $\mu = 40\Delta$ . Nonlocal conductance in the AAR regime for (c)  $Z = 0$  and (d)  $Z = 1$ , with  $eV = 0.2\Delta$  and  $\mu = 0$ . The location of the open surface of nodal line semimetal is  $x_0 = 200$  nm. All the other parameters are the same as those in Fig. 3.

cesses.

Since different types of AR are featured by their lateral velocities, it is difficult to identify them by the longitudinal current flow across the junction. Instead, they can be visibly revealed by the hole propagation in the  $y$ - $z$  plane, which manifests in the nonlocal transport measurement. Consider the two-terminal setup in Fig. 4(a) on top of the nodal line semimetal, which involves a local electrode at  $\mathbf{x}_l = (-x_0, 0, 0)$  and a movable STM tip at  $\mathbf{x}_s = (-x_0, y, z)$ . An electron wave packet is injected from the local electrode which involves contribution of all available  $(k_y, k_z)$  channels, then gets Andreev reflected as a hole wave packet, and finally reaches the tip. For the RAR process, both lateral velocities change sign, so that the hole retraces the path of the electron, which is localized in the  $y$ - $z$  plane. In contrast, only one lateral velocity component is inverted in the AAR, which indicates that the hole wave packet exhibits a ridge structure, i.e., localized in one direction while extended in the other [cf. Fig. 4(a)].

In what follows we calculate the nonlocal conductance using the Green's function method. The electron coupling between the local terminals and the nodal line semimetal is described by tunneling Hamiltonian  $H_T = \sum_{p,\alpha=l,s} t_\alpha c_{p\alpha}^\dagger \Psi(\mathbf{x}_\alpha) + h.c.$ , where  $t_\alpha$  is the tunneling strength in the  $\alpha$  terminal,  $c_{p\alpha}^\dagger$  is the creation operator of electron with momentum  $p$  in the  $\alpha$  terminal, and  $\Psi(\mathbf{x})$  is the field operator in the nodal line semimetal. The nonlocal conductance at zero temperature between

the electrode and the STM tip is given by [38]

$$\sigma(eV) = \frac{e^2}{h} \sum_{a,b} \zeta_{ab} \text{Tr}[\Gamma_{ls}^a \mathbf{G}_{ab}^R \Gamma_s^b \mathbf{G}_{ba}^A], \quad (6)$$

where  $\mathbf{G}^{R,A}$  is the retarded or advanced Green's function,  $\Gamma_{l,s}$  is the linewidth function, and subscripts  $a, b = e_{1,2}, h_{1,2}$  denote the electron and hole components.  $\zeta_{ab} = -1$  if  $a, b$  are both electron/hole states; otherwise,  $\zeta_{ab} = 1$ . In the weak coupling limit, the correction to the Green's function due to multiple tunneling can be neglected. Then the retarded Green's function is constructed by the scattering matrix through [38]

$$\mathbf{G}_{ba}^R(\mathbf{x}', \mathbf{x}, E) = -\frac{i}{4\pi^2} \sum_{k_y, k_z} \frac{\gamma_a^b}{\hbar v_a} e^{i(\gamma_{yz} - \gamma_x)} |b\rangle \langle a|, \quad (7)$$

where the phase factors are defined by  $\gamma_{yz} = k_y(y' - y) + k_z(z' - z)$  and  $\gamma_x = k_a x + k_b x'$ . The advanced Green's function is obtained by  $\mathbf{G}_{ab}^A(\mathbf{x}, \mathbf{x}', E) = [\mathbf{G}_{ba}^R(\mathbf{x}', \mathbf{x}, E)]^*$ . The linewidth function in Eq. (6) is given by  $\Gamma_\alpha^R(\mathbf{x}_1, \mathbf{x}_2, E) = 2\pi\rho_\alpha |t_\alpha|^2 \delta(\mathbf{x}_1 - \mathbf{x}_\alpha) \delta(\mathbf{x}_2 - \mathbf{x}_\alpha)$ , where  $\rho_\alpha$  is the density of states at Fermi energy in the  $\alpha$  terminal.

We solve Eq. (6) numerically and the results of reduced conductance  $\sigma/\sigma_0$  are shown in Fig. 4, with  $\sigma_0(eV) = (e^2/h) |2\pi t_l t_s \rho_N|^2 \rho_l \rho_s$  and  $\rho_N = 2\pi k_0 (\mu + eV) / (\alpha \hbar^2 v_0^2)$  as the density of states in the nodal line semimetal. In the intra-band AR regime ( $E, \Delta \ll \mu$ ), the current is dominated by the RAR and the conductance exhibits a peak structure localized in both  $y$  and  $z$  directions [41]; see Fig. 4(b). In the inter-band AR regime ( $E, \Delta \gg \mu$ ), the AAR dominates the nonlocal transport, and the conductance exhibits a ridge structure along the  $z$  direction as expected; see Fig. 4(c). For  $U \neq 0$ , the interface barrier reduces the AAR while enhances the normal electron reflection [cf. Fig. 3(f)]. Such an effect is enhanced with  $k_z$  increased, and similar anomalous normal reflection  $B_{21}$  can even invert the sign of conductance at the edges of the ridge, as shown in Fig. 4(d). Even so, the ridge structural feature still persists, and the effect of interface barrier can be greatly weakened by setting the energy of incident electron as close as possible to  $\Delta$ , where the Andreev resonance occurs [cf. Fig. 3(f)]. We conclude that the nonlocal conductance spectra provide an effective way to identify different types of AR.

It is worthwhile to discuss the experimental implementation and potential application of our proposal. (i) The main building block, Fermi torus has been reported in doped nodal line semimetals [18–21] as well as the low-density Rashba gases [42–46]. (ii) The local electrode of a few nanometer size can be fabricated by various state-of-the-art techniques [47–49]. The spatially resolved conductance measurements can be achieved by a single STM biased with the electrode. The measurements can also be implemented by the multi-tip STM technique [50, 51],



which has been used to perform nonlocal transport measurements [52–55]. Both the scale of the local electrode and the accessible spacing between two STM tips can be much smaller than the spreading of the ridge structure in the  $z$  direction [cf. Fig. 4(c)] which ensure a high resolution of the signature. (iii) High-quality samples of nodal line semimetal with ultrahigh mobility and clean surface have been synthesized, which ensures a long mean free path [19, 56–58]. The disorder and interface roughness can break the lateral translational symmetry and lead to diffusion, which will reduce the spatial resolution of the signal. (iv) Apart from its novel phenomenology, AAR also provides an effective way to manipulate Cooper pair splitting process, which may have important applications in solid-state quantum information processing [13–15].

We thank Fengqi Song, Shaochun Li, Jie Shen, Bin Cheng and Libo Gao for helpful discussions on the experimental implementation of our proposal. This work was supported by the National Natural Science Foundation of China under Grant No. 12074172 (W.C.) and No. 11804130 (W.L.), the startup grant at Nanjing University (W.C.), the State Key Program for Basic Researches of China under Grants No. 2017YFA0303203 (D.Y.X.) and the Excellent Programme at Nanjing University.

---

\* Corresponding author: pchenweis@gmail.com

- [1] AF Andreev, “Thermal conductivity of the intermediate state of superconductors ii,” *Sov. Phys. JETP* **19**, 1228 (1964).
- [2] G. E. Blonder, M. Tinkham, and T. M. Klapwijk, “Transition from metallic to tunneling regimes in superconducting microconstrictions: Excess current, charge imbalance, and supercurrent conversion,” *Phys. Rev. B* **25**, 4515–4532 (1982).
- [3] Chr. Bruder, “Andreev scattering in anisotropic superconductors,” *Phys. Rev. B* **41**, 4017–4032 (1990).
- [4] Yukio Tanaka and Satoshi Kashiwaya, “Theory of tunneling spectroscopy of  $d$ -wave superconductors,” *Phys. Rev. Lett.* **74**, 3451–3454 (1995).
- [5] Satoshi Kashiwaya and Yukio Tanaka, “Tunnelling effects on surface bound states in unconventional superconductors,” *Reports on Progress in Physics* **63**, 1641 (2000).
- [6] M. J. M. de Jong and C. W. J. Beenakker, “Andreev reflection in ferromagnet-superconductor junctions,” *Phys. Rev. Lett.* **74**, 1657–1660 (1995).
- [7] R. J. Soulen, J. M. Byers, M. S. Osofsky, B. Nadgorny, T. Ambrose, S. F. Cheng, P. R. Broussard, C. T. Tanaka, J. Nowak, J. S. Moodera, A. Barry, and J. M. D. Coey, “Measuring the spin polarization of a metal with a superconducting point contact,” *Science* **282**, 85–88 (1998), <https://science.sciencemag.org/content/282/5386/85.full.pdf>.
- [8] C. W. J. Beenakker, “Specular andreev reflection in graphene,” *Phys. Rev. Lett.* **97**, 067007 (2006).
- [9] Qingyun Zhang, Deyi Fu, Baigeng Wang, R. Zhang, and D. Y. Xing, “Signals for specular andreev reflection,” *Phys. Rev. Lett.* **101**, 047005 (2008).
- [10] Wei Chen, Liang Jiang, R. Shen, L. Sheng, BG Wang, and DY Xing, “Specular andreev reflection in inversion-symmetric weyl semimetals,” *EPL (Europhysics Letters)* **103**, 27006 (2013).
- [11] K. T. Law, Patrick A. Lee, and T. K. Ng, “Majorana fermion induced resonant andreev reflection,” *Phys. Rev. Lett.* **103**, 237001 (2009).
- [12] V. Mourik, K. Zuo, S. M. Frolov, S. R. Plissard, E. P. A. M. Bakkers, and L. P. Kouwenhoven, “Signatures of majorana fermions in hybrid superconductor-semiconductor nanowire devices,” *Science* **336**, 1003–1007 (2012), <https://science.sciencemag.org/content/336/6084/1003.full.pdf>.
- [13] Patrik Recher, Eugene V. Sukhorukov, and Daniel Loss, “Andreev tunneling, coulomb blockade, and resonant transport of nonlocal spin-entangled electrons,” *Phys. Rev. B* **63**, 165314 (2001).
- [14] Gordey B Lesovik, Thierry Martin, and Gianni Blatter, “Electronic entanglement in the vicinity of a superconductor,” *The European Physical Journal B-Condensed Matter and Complex Systems* **24**, 287–290 (2001).
- [15] Lukas Hofstetter, Sa Csonka, Jesper Nygård, and C Schönenberger, “Cooper pair splitter realized in a two-quantum-dot y-junction,” *Nature* **461**, 960–963 (2009).
- [16] Matthias Eschrig, “Spin-polarized supercurrents for spintronics,” *Phys. Today* **64**, 43 (2011).
- [17] Dmitri K Efetov, L Wang, C Handschin, KB Efetov, J Shuang, R Cava, T Taniguchi, K Watanabe, J Hone, CR Dean, *et al.*, “Specular interband andreev reflections at van der waals interfaces between graphene and nbse 2,” *Nature Physics* **12**, 328–332 (2016).
- [18] Eve Emmanouilidou, Bing Shen, Xiaoyu Deng, Tay-Rong Chang, Aoshuang Shi, Gabriel Kotliar, Su-Yang Xu, and Ni Ni, “Magnetotransport properties of the single-crystalline nodal-line semimetal candidates  $Catx(t = Ag, Cd; x = As, Ge)$ ,” *Phys. Rev. B* **95**, 245113 (2017).
- [19] Daichi Takane, Kosuke Nakayama, Seigo Souma, Taichi Wada, Yoshihiko Okamoto, Koshi Takenaka, Youichi Yamakawa, Ai Yamakage, Taichi Mitsuhashi, Koji Horiba, *et al.*, “Observation of dirac-like energy band and ring-torus fermi surface associated with the nodal line in topological insulator caagas,” *npj Quantum Materials* **3**, 1–6 (2018).
- [20] Hishiro T. Hirose, Taichi Terashima, Taichi Wada, Yoshitaka Matsushita, Yoshihiko Okamoto, Koshi Takenaka, and Shinya Uji, “Real spin and pseudospin topologies in the noncentrosymmetric topological nodal-line semimetal caagas,” *Phys. Rev. B* **101**, 245104 (2020).
- [21] Y. H. Kwan, P. Reiss, Y. Han, M. Bristow, D. Prabhakaran, D. Graf, A. McCollam, S. A. Parameswaran, and A. I. Coldea, “Quantum oscillations probe the fermi surface topology of the nodal-line semimetal caagas,” *Phys. Rev. Research* **2**, 012055 (2020).
- [22] A. A. Burkov, M. D. Hook, and Leon Balents, “Topological nodal semimetals,” *Phys. Rev. B* **84**, 235126 (2011).
- [23] Youngkuk Kim, Benjamin J. Wieder, C. L. Kane, and Andrew M. Rappe, “Dirac line nodes in inversion-symmetric crystals,” *Phys. Rev. Lett.* **115**, 036806 (2015).
- [24] Rui Yu, Hongming Weng, Zhong Fang, Xi Dai, and Xiao Hu, “Topological node-line semimetal and dirac semimetal state in antiperovskite  $\text{Cu}_3\text{PdN}$ ,” *Phys. Rev. Lett.* **115**, 036807 (2015).
- [25] T. T. Heikkilä, N. B. Kopnin, and G. E. Volovik, “Flat bands in topological media,” *JETP Letters* **94**, 233

- (2011).
- [26] Hongming Weng, Yunye Liang, Qiunan Xu, Rui Yu, Zhong Fang, Xi Dai, and Yoshiyuki Kawazoe, “Topological node-line semimetal in three-dimensional graphene networks,” *Phys. Rev. B* **92**, 045108 (2015).
  - [27] Yuanping Chen, Yuee Xie, Shengyuan A. Yang, Hui Pan, Fan Zhang, Marvin L. Cohen, and Shengbai Zhang, “Nanostructured carbon allotropes with weyl-like loops and points,” *Nano Letters* **15**, 6974–6978 (2015), pMID: 26426355, <http://dx.doi.org/10.1021/acs.nanolett.5b02978>.
  - [28] Minggang Zeng, Chen Fang, Guoqing Chang, Yu-An Chen, Timothy Hsieh, Arun Bansil, Hsin Lin, and Liang Fu, “Topological semimetals and topological insulators in rare earth monpnictides,” arXiv:1504.03492 [cond-mat] (2015), arXiv: 1504.03492.
  - [29] Chen Fang, Yige Chen, Hae-Young Kee, and Liang Fu, “Topological nodal line semimetals with and without spin-orbital coupling,” *Phys. Rev. B* **92**, 081201 (2015).
  - [30] Ai Yamakage, Youichi Yamakawa, Yukio Tanaka, and Yoshihiko Okamoto, “Line-node dirac semimetal and topological insulating phase in noncentrosymmetric pnictides caagx ( $x = p, as$ ),” *Journal of the Physical Society of Japan* **85**, 013708 (2016), <https://doi.org/10.7566/JPSJ.85.013708>.
  - [31] Lilia S. Xie, Leslie M. Schoop, Elizabeth M. Seibel, Quinn D. Gibson, Weiwei Xie, and Robert J. Cava, “A new form of  $ca_3p_2$  with a ring of dirac nodes,” *APL Materials* **3**, 083602 (2015), <http://dx.doi.org/10.1063/1.4926545>.
  - [32] Y.-H. Chan, Ching-Kai Chiu, M. Y. Chou, and Andreas P. Schnyder, “ $ca_3p_2$ ,” *Phys. Rev. B* **93**, 205132 (2016).
  - [33] Jianzhou Zhao, Rui Yu, Hongming Weng, and Zhong Fang, “Topological node-line semimetal in compressed black phosphorus,” *Phys. Rev. B* **94**, 195104 (2016).
  - [34] Guang Bian, Tay-Rong Chang, Hao Zheng, Saavanth Velury, Su-Yang Xu, Titus Neupert, Ching-Kai Chiu, Shin-Ming Huang, Daniel S. Sanchez, Ilya Belopolski, Nasser Alidoust, Peng-Jen Chen, Guoqing Chang, Arun Bansil, Horng-Tay Jeng, Hsin Lin, and M. Zahid Hasan, “Drumhead surface states and topological nodal-line fermions in  $tlase_2$ ,” *Phys. Rev. B* **93**, 121113 (2016).
  - [35] Guang Bian, Tay-Rong Chang, Raman Sankar, Su-Yang Xu, Hao Zheng, Titus Neupert, Ching-Kai Chiu, Shin-Ming Huang, Guoqing Chang, Ilya Belopolski, Daniel S. Sanchez, Madhab Neupane, Nasser Alidoust, Chang Liu, BaoKai Wang, Chi-Cheng Lee, Horng-Tay Jeng, Chenglong Zhang, ZhuJun Yuan, Shuang Jia, Arun Bansil, Fangcheng Chou, Hsin Lin, and M. Zahid Hasan, “Topological nodal-line fermions in spin-orbit metal  $pbtase_2$ ,” **7**, 10556 EP – (2016), article.
  - [36] Wei Chen, Hai-Zhou Lu, and Oded Zilberberg, “Weak localization and antilocalization in nodal-line semimetals: Dimensionality and topological effects,” *Phys. Rev. Lett.* **122**, 196603 (2019).
  - [37] Cequn Li, C. M. Wang, Bo Wan, Xiangang Wan, Hai-Zhou Lu, and X. C. Xie, “Rules for phase shifts of quantum oscillations in topological nodal-line semimetals,” *Phys. Rev. Lett.* **120**, 146602 (2018).
  - [38] See Supplemental Material at xxx for the illustration of the transition between different types of Andreev reflection, construction of Green’s function by the scattering matrix, nonlocal conductance calculated by Green’s function method and results of longitudinal conductance across the junction, which includes Refs [2, 8, 39, 40].
  - [39] Massimiliano Di Ventra, *Electrical transport in nanoscale systems* (Cambridge University Press, 2008).
  - [40] Antti-Pekka Jauho, Ned S. Wingreen, and Yigal Meir, “Time-dependent transport in interacting and noninteracting resonant-tunneling systems,” *Phys. Rev. B* **50**, 5528–5544 (1994).
  - [41] In reality, the RAR induced peak structure of the conductance is covered by the electrode, so that it cannot be measured by the STM tip. Instead, it can be probed directly through the local current and revealed in the local conductance spectra.
  - [42] Fei-Xiang Xiang, Xiao-Lin Wang, Menno Veldhorst, Shi-Xue Dou, and Michael S. Fuhrer, “Observation of topological transition of fermi surface from a spindle torus to a torus in bulk rashba spin-split bitecl,” *Phys. Rev. B* **92**, 035123 (2015).
  - [43] Gabriel Landolt, Sergey V. Eremeev, Yury M. Koroteev, Bartosz Slomski, Stefan Muff, Titus Neupert, Masaki Kobayashi, Vladimir N. Strocov, Thorsten Schmitt, Ziya S. Aliev, Mahammad B. Babanly, Imamaddin R. Amirasanov, Evgueni V. Chulkov, Jürg Osterwalder, and J. Hugo Dil, “Disentanglement of surface and bulk rashba spin splittings in noncentrosymmetric bitei,” *Phys. Rev. Lett.* **109**, 116403 (2012).
  - [44] A. Crepaldi, L. Moreschini, G. Autès, C. Tournier-Colletta, S. Moser, N. Virk, H. Berger, Ph. Bugnon, Y. J. Chang, K. Kern, A. Bostwick, E. Rotenberg, O. V. Yazyev, and M. Grioni, “Giant ambipolar rashba effect in the semiconductor bitei,” *Phys. Rev. Lett.* **109**, 096803 (2012).
  - [45] E. Cappelluti, C. Grimaldi, and F. Marsiglio, “Topological change of the fermi surface in low-density rashba gases: Application to superconductivity,” *Phys. Rev. Lett.* **98**, 167002 (2007).
  - [46] Kazuhiro Tsutsui and Shuichi Murakami, “Spin-torque efficiency enhanced by rashba spin splitting in three dimensions,” *Phys. Rev. B* **86**, 115201 (2012).
  - [47] DM Kolb, R Ullmann, and T Will, “Nanofabrication of small copper clusters on gold (111) electrodes by a scanning tunneling microscope,” *Science* **275**, 1097–1099 (1997).
  - [48] Christophe Vieu, F Carcenac, A Pepin, Y Chen, M Mejias, A Lebib, L Manin-Ferlazzo, L Couraud, and H Launois, “Electron beam lithography: resolution limits and applications,” *Applied surface science* **164**, 111–117 (2000).
  - [49] Martin Fuechsle, Jill A Miwa, Suddhasatta Mahapatra, Hoon Ryu, Sunhee Lee, Oliver Warschkow, Lloyd CL Hollenberg, Gerhard Klimeck, and Michelle Y Simmons, “A single-atom transistor,” *Nature nanotechnology* **7**, 242–246 (2012).
  - [50] Tomonobu Nakayama, Osamu Kubo, Yoshitaka Shingaya, Seiji Higuchi, Tsuyoshi Hasegawa, Chun-Sheng Jiang, Taichi Okuda, Yuji Kuwahara, Kazuhiro Takami, and Masakazu Aono, “Development and application of multiple-probe scanning probe microscopes,” *Advanced materials* **24**, 1675–1692 (2012).
  - [51] An-Ping Li, Kendal W Clark, X-G Zhang, and Arthur P Baddorf, “Electron transport at the nanometer-scale spatially revealed by four-probe scanning tunneling microscopy,” *Advanced Functional Materials* **23**, 2509–2524 (2013).

- [52] Jens Baringhaus, Ming Ruan, Frederik Edler, Antonio Tejeda, Muriel Sicot, Amina Taleb-Ibrahimi, An-Ping Li, Zhigang Jiang, Edward H Conrad, Claire Berger, *et al.*, “Exceptional ballistic transport in epitaxial graphene nanoribbons,” *Nature* **506**, 349–354 (2014).
- [53] Sven Just, Marcus Blab, Stefan Korte, Vasily Cherepanov, Helmut Soltner, and Bert Voigtländer, “Surface and step conductivities on si(111) surfaces,” *Phys. Rev. Lett.* **115**, 066801 (2015).
- [54] Saban M. Hus, X.-G. Zhang, Giang D. Nguyen, Wonhee Ko, Arthur P. Baddorf, Yong P. Chen, and An-Ping Li, “Detection of the spin-chemical potential in topological insulators using spin-polarized four-probe stm,” *Phys. Rev. Lett.* **119**, 137202 (2017).
- [55] Marek Kolmer, Pedro Brandimarte, Jakub Lis, Rafal Zuzak, Szymon Godlewski, Hiroyo Kawai, Aran Garcia-Lekue, Nicolas Lorente, Thomas Frederiksen, Christian Joachim, *et al.*, “Electronic transport in planar atomic-scale structures measured by two-probe scanning tunneling spectroscopy,” *Nature communications* **10**, 1–10 (2019).
- [56] Leslie M. Schoop, Mazhar N. Ali, Carola Straßer, Andreas Topp, Andrei Varykhalov, Dmitry Marchenko, Viola Duppel, Stuart S. P. Parkin, Bettina V. Lotsch, and Christian R. Ast, “Dirac cone protected by non-symmorphic symmetry and three-dimensional Dirac line node in ZrSiS,” **7**, 11696 (2016).
- [57] Raman Sankar, G Peramaiyan, I Panneer Muthuselvam, Christopher J Butler, Klauss Dimitri, Madhab Neupane, G Narsinga Rao, M-T Lin, and FC Chou, “Crystal growth of dirac semimetal zrsi with high magnetoresistance and mobility,” *Scientific reports* **7**, 40603 (2017).
- [58] Ratnadwip Singha, Arnab Kumar Pariari, Biswarup Satpati, and Prabhat Mandal, “Large nonsaturating magnetoresistance and signature of nondegenerate dirac nodes in zrsi,” *Proceedings of the National Academy of Sciences* **114**, 2468–2473 (2017).

## SUPPLEMENTAL MATERIAL FOR “ANOMALOUS ANDREEV REFLECTION ON A TORUS-SHAPED FERMI SURFACE”

### Transition between different types of Andreev reflection

Smooth transition of real-space trajectories between different types of AR is illustrated in Fig. S.1. For the dominant AR processes with  $k_x > 0$ , RAR gradually evolves into AAR by inverting  $v_z$  as the chemical potential reduces from  $\mu \gg \Delta$  to zero. Meanwhile, weak AR processes with  $k_x < 0$  undergoes a transition from another type of AAR to SAR by inverting  $v_z$  as well.

### Green’s function constructed by the scattering matrix

Consider a two-terminal system as the junction in the main text, the scattering states for a particle incident from the left and right side write

$$\begin{aligned} |L\rangle_i &= \begin{cases} |i\rangle_{\rightarrow} + \sum_j r_i^j |j\rangle_{\leftarrow}, & x < 0 \\ \sum_n t_i^n |n\rangle_{\rightarrow}, & x > 0 \end{cases} \\ |R\rangle_m &= \begin{cases} |m\rangle_{\leftarrow} + \sum_n r_m^n |n\rangle_{\rightarrow}, & x > 0 \\ \sum_j t_m^j |j\rangle_{\leftarrow}, & x < 0 \end{cases} \end{aligned} \quad (\text{S.1})$$

where  $i, n$  ( $j, m$ ) denote the right-moving (left-moving) modes on the left and right side, respectively. For a fixed energy, these labels specify the spinor components such as  $|e_{1,2}\rangle, |h_{1,2}\rangle$  and the momentum of the states. The Eq. (3) in the main text is a special case of  $|L\rangle_i$ .

In order to make the scattering matrix unitary, the scattering coefficients should include the ratio of velocity in the  $x$ -direction. We revise the scattering states to

$$\begin{aligned} |\tilde{L}\rangle_i &= \begin{cases} |\tilde{i}\rangle_{\rightarrow} + \sum_j \tilde{r}_i^j |\tilde{j}\rangle_{\leftarrow}, & x < 0 \\ \sum_n \tilde{t}_i^n |\tilde{n}\rangle_{\rightarrow}, & x > 0 \end{cases} \\ |\tilde{R}\rangle_m &= \begin{cases} |\tilde{m}\rangle_{\leftarrow} + \sum_n \tilde{r}_m^n |\tilde{n}\rangle_{\rightarrow}, & x > 0 \\ \sum_j \tilde{t}_m^j |\tilde{j}\rangle_{\leftarrow}, & x < 0 \end{cases} \end{aligned} \quad (\text{S.2})$$

with

$$\begin{aligned} |\tilde{i}\rangle &= |i\rangle / \sqrt{\hbar v_i}, & |\tilde{j}\rangle &= |j\rangle / \sqrt{\hbar v_j}, \dots \\ \tilde{r}_i^j &= r_i^j \sqrt{v_j / v_i}, & \tilde{t}_i^n &= t_i^n \sqrt{v_n / v_i}, \dots \end{aligned} \quad (\text{S.3})$$

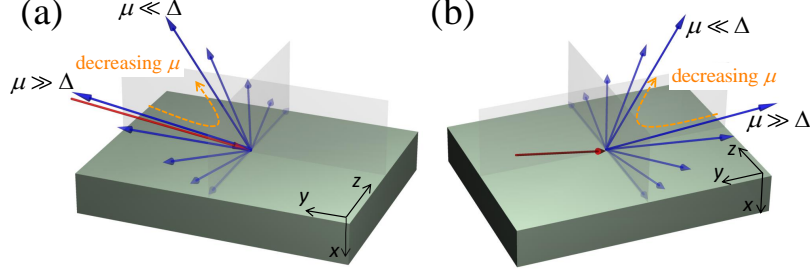


FIG. S.1. (a) RAR-to-AAR transition with  $k_x > 0$  and (b) AAR-to-SAR transition with  $k_x < 0$  as the chemical potential  $\mu$  decreases.

In such a way, we obtain the unitary scattering matrix

$$S = \begin{pmatrix} \tilde{r} & \tilde{t}' \\ \tilde{t} & \tilde{r}' \end{pmatrix}, \quad SS^\dagger = I. \quad (\text{S.4})$$

We expand the Green's function under the basis of scattering states (S.2). For  $x, x' < 0$ , the retarded Green's function is calculated by [39]

$$\begin{aligned} \mathbf{G}^R(\mathbf{x}', \mathbf{x}, \omega) &= \langle \mathbf{x}' | \frac{1}{\omega - H + i0^+} | \mathbf{x} \rangle \\ &= \sum_i \int dE_i \frac{\langle \mathbf{x}' | \tilde{L} \rangle_i \langle \tilde{L} | \mathbf{x} \rangle}{\omega - E_i + i0^+} + \sum_m \int dE_m \frac{\langle \mathbf{x}' | \tilde{R} \rangle_m \langle \tilde{R} | \mathbf{x} \rangle}{\omega - E_m + i0^+} \\ &= \int dE \frac{\sum_i [\tilde{\psi}_i(\mathbf{x}') + \sum_j \tilde{r}_i^j \tilde{\psi}_j(\mathbf{x}')] [\tilde{\psi}_i^*(\mathbf{x}) + \sum_{j'} \tilde{r}_i^{j'*} \tilde{\psi}_{j'}^*(\mathbf{x})] + \sum_m [\sum_j \tilde{t}_m^j \tilde{\psi}_j(\mathbf{x}')] [\sum_{j'} \tilde{t}_m^{j'*} \tilde{\psi}_{j'}^*(\mathbf{x})]}{\omega - E + i0^+} \\ \mathbf{G}^R(\mathbf{x}', \mathbf{x}, \omega) &= \int dE \frac{\sum_i \tilde{\psi}_i(\mathbf{x}') \tilde{\psi}_i^*(\mathbf{x}) + \sum_j \tilde{\psi}_j(\mathbf{x}') \tilde{\psi}_j^*(\mathbf{x})}{\omega - E + i0^+} + \int dE \frac{\sum_{ij} \tilde{r}_i^j \tilde{\psi}_i(\mathbf{x}') \tilde{\psi}_j^*(\mathbf{x}) + \tilde{r}_i^j \tilde{\psi}_j(\mathbf{x}') \tilde{\psi}_i^*(\mathbf{x})}{\omega - E + i0^+}. \end{aligned} \quad (\text{S.5})$$

In the last step, we have used the unitary condition  $\sum_{jj'} (\tilde{t}' \tilde{t}'^\dagger + \tilde{r} \tilde{r}^\dagger) = \delta_{jj'}$ . The first term of Eq. (S.5) describes the free propagation of particle, which has no contribution to the nonlocal transport between the local electrode and the STM tip and thus can be dropped. Calculating the remaining term using the residue theorem yields

$$\mathbf{G}^R(\mathbf{x}', \mathbf{x}, \omega) = -2\pi i \sum_{ij} \tilde{r}_i^j \tilde{\psi}_j(\mathbf{x}') \tilde{\psi}_i^*(\mathbf{x}) \quad (\text{S.6})$$

The wave functions take the form of

$$\begin{aligned} \tilde{\psi}_i(\mathbf{x}) &= \frac{1}{\sqrt{2\pi\hbar v_i}} \chi_i(y, z) e^{ik_i x}, \\ \tilde{\psi}_j(\mathbf{x}') &= \frac{1}{\sqrt{2\pi\hbar v_j}} \chi_j(y', z') e^{-ik_j x'}, \end{aligned} \quad (\text{S.7})$$

with the transverse modes being labeled by the momentum  $k_y, k_z$  as

$$\begin{aligned} \chi_i(y, z) &= \frac{1}{2\pi} |a\rangle e^{i(k_y y + k_z z)}, \\ \chi_j(y', z') &= \frac{1}{2\pi} |b\rangle e^{i(k_y y' + k_z z')}, \end{aligned} \quad (\text{S.8})$$

where  $|a\rangle, |b\rangle = |e_{1,2}\rangle, |h_{1,2}\rangle$  are the spinor part of the wave function.

Inserting the wave functions into the expression of Green's function and given the conservation of transverse momentum during scattering yields

$$\mathbf{G}_{ba}^R(\mathbf{x}', \mathbf{x}, E) = -\frac{i}{4\pi^2} \sum_{k_y, k_z} \frac{r_a^b}{\hbar v_a} e^{i[k_y(y'-y) + k_z(z'-z)]} e^{-i[k_a x + k_b x']} |b\rangle \langle a|, \quad (\text{S.9})$$

which is Eq. (7) in the main text, with  $k_{a,b} = k_{a,b}(k_y, k_z, E)$ ,  $v_{a,b} = v_{a,b}(k_y, k_z, E)$



### Green's function formula of nonlocal conductance

Consider the local electrode and STM tip coupled with the nodal line semimetal as shown in Fig. 4(a) of the main text. The whole system is composed of two local terminals and the central scattering region: the nodal line semimetal-superconductor junction. Following Ref. [40], we derive the general expression of the nonlocal conductance for the system which contains a superconductor. The whole Hamiltonian in Nambu space is

$$\begin{aligned} H_L &= \sum_{\alpha=l,s} \sum_p \tilde{c}_{p\alpha}^\dagger h_{p\alpha} \tilde{c}_{p\alpha}, \\ H_0 &= \sum_{mn} \tilde{d}_m^\dagger h_{mn}^s \tilde{d}_n, \\ H_T &= \sum_{\alpha=l,s} \sum_{p,n} [\tilde{c}_{p\alpha}^\dagger t_{p\alpha,n} \tilde{d}_n + H.c.], \end{aligned} \quad (\text{S.10})$$

where  $H_L$  is for the local electrode and STM tip,  $H_0$  corresponds to the nodal line semimetal-superconductor junction and  $H_T$  is the coupling between them. The single-particle Hamiltonian is defined as  $h_{p\alpha} = \begin{pmatrix} \epsilon_{p\alpha} & 0 \\ 0 & -\epsilon_{-p\alpha} \end{pmatrix} =$

$\begin{pmatrix} \epsilon_{p\alpha}^e & 0 \\ 0 & \epsilon_{p\alpha}^h \end{pmatrix}$ ,  $t_{p\alpha,n} = \begin{pmatrix} T_{p\alpha,n} & 0 \\ 0 & -T_{-p\alpha,n}^* \end{pmatrix} = \begin{pmatrix} t_{p\alpha,n}^e & 0 \\ 0 & t_{p\alpha,n}^h \end{pmatrix}$ , and the Nambu spinors are defined by  $\tilde{c}_{p\alpha} = (\tilde{c}_{p\alpha}^e, \tilde{c}_{p\alpha}^h)^T = (c_{p\alpha\uparrow}, c_{-p\alpha\downarrow}^\dagger)^T$ ,  $\tilde{d}_n = (\tilde{d}_n^e, \tilde{d}_n^h)^T = (d_{n\uparrow}, d_{n\downarrow}^\dagger)^T$ . All energies and coupling strength are time-independent. The current in the STM tip is defined by

$$\begin{aligned} J_s(t) &= -e \langle \dot{N}_s \rangle = -\frac{ie}{\hbar} \langle [H, N_s] \rangle \\ &= \frac{ie}{\hbar} \sum_{pn} [\langle \tilde{c}_{ps}^\dagger(t) \tau_z t_{ps,n} \tilde{d}_n(t) \rangle - \langle \tilde{d}_n^\dagger(t) \tau_z t_{ps,n}^* \tilde{c}_{ps}(t) \rangle]. \end{aligned} \quad (\text{S.11})$$

Define the lesser Green's function

$$G_{n,p\alpha}^{<\mu\nu}(t, t') \equiv i \langle \tilde{c}_{p\alpha}^{\dagger\nu}(t') \tilde{d}_n^\mu(t) \rangle, \quad (\text{S.12})$$

where the superscripts  $\mu, \nu$  denote the electron-hole components. Using the Green's function, the current is expressed as

$$J_s(t) = \frac{2e}{\hbar} \text{Re} \left\{ \sum_{pn} \text{Tr} [\tau_z t_{ps,n}(t) G_{n,ps}^{<}(t, t)] \right\}. \quad (\text{S.13})$$

The lesser Green's function can be obtained by analytic continuation on the following contour-ordered Green's function

$$G_{n,p\alpha}^{\mu\nu}(\tau, \tau') = \sum_m \int \tau_1 G_{nm}^{\mu\nu}(\tau, \tau_1) t_{p\alpha,m}^{\nu*}(\tau_1) g_{p\alpha}^\nu(\tau_1, \tau'), \quad (\text{S.14})$$

which yields [40]

$$G_{n,p\alpha}^{<\mu\nu}(t, t') = \sum_m \int dt_1 \left[ G_{nm}^{R\mu\nu}(t, t_1) t_{p\alpha,m}^{\nu*}(t_1) g_{p\alpha}^{<\nu}(t_1, t') + G_{nm}^{<\mu\nu}(t, t_1) t_{p\alpha,m}^{\nu*}(t_1) g_{p\alpha}^{A\nu}(t_1, t') \right]. \quad (\text{S.15})$$

The bare Green's function in the lead is diagonal in Nambu space, which is

$$\begin{aligned} g_{p\alpha}^{<\nu}(t, t') &= i \langle \tilde{c}_{p\alpha}^{\dagger\nu}(t') \tilde{c}_{p\alpha}^\nu(t) \rangle = i f_\alpha^\nu(\epsilon_{p\alpha}^\nu) e^{-i\epsilon_{p\alpha}^\nu(t-t')}, \\ g_{p\alpha}^{R,A\nu}(t, t') &= \mp i \theta(\pm t \mp t') \langle [\tilde{c}_{p\alpha}^\nu(t), \tilde{c}_{p\alpha}^{\dagger\nu}(t')]_{\pm} \rangle = \mp i \theta(\pm t \mp t') e^{-i\epsilon_{p\alpha}^\nu(t-t')}. \end{aligned} \quad (\text{S.16})$$

For the  $\alpha$  terminal, the hole distribution function  $f_\alpha^h$  is related to that of electron via  $f_\alpha^h(\epsilon_{p\alpha}^h) = 1 - f_\alpha^e(\epsilon_{-p\alpha})$ . As the electrode is biased by a voltage  $eV$ , the electron distribution is  $f_\alpha^e(\omega) = f_0(\omega - eV)$  and the hole distribution is  $f_\alpha^h(\omega) = f_0(\omega + eV)$ , with  $f_0(\omega) = 1/(e^{\beta\omega} + 1)$  being the Fermi-Dirac distribution function. The current Eq.

(S.13) includes only the diagonal elements  $[\nu = 1, 2 \text{ (} e, h \text{)}]$  of the Green's function, which can be labeled by a single superscript  $\nu$  as

$$G_{n,p\alpha}^{<\nu}(t, t') = \sum_m \int dt_1 t_{p\alpha,m}^{\nu*} \left[ G_{nm}^{R\nu}(t, t_1) i f_{\alpha}^{\nu}(\epsilon_{p\alpha}^{\nu}) e^{-i\epsilon_{p\alpha}^{\nu}(t_1-t')} + G_{nm}^{<\nu}(t, t_1) i \theta(-t_1 + t') e^{-i\epsilon_{p\alpha}^{\nu}(t_1-t')} \right]. \quad (\text{S.17})$$

Then the current reduces to

$$\begin{aligned} J_s(t) &= \frac{2e}{\hbar} \text{Im} \left\{ \sum_{pnm\nu} (-1)^{\nu} t_{ps,n}^{\nu} \int_{-\infty}^t dt_1 t_{ps,m}^{\nu*} e^{-i\epsilon_{ps}^{\nu}(t_1-t)} \left[ G_{nm}^{R\nu}(t, t_1) f_s^{\nu}(\epsilon_{ps}^{\nu}) + G_{nm}^{<\nu}(t, t_1) \right] \right\} \\ &= \frac{2e}{\hbar} \text{Im} \left\{ \sum_{nm\nu} (-1)^{\nu} \int d\epsilon_s^{\nu} \rho_s^{\nu}(\epsilon_s^{\nu}) t_{s,n}^{\nu}(\epsilon_s^{\nu}) \int_{-\infty}^t dt_1 e^{-i\epsilon_s^{\nu}(t_1-t)} t_{s,m}^{\nu*}(\epsilon_s^{\nu}) \left[ G_{nm}^{R\nu}(t - t_1) f_s^{\nu}(\epsilon_s^{\nu}) + G_{nm}^{<\nu}(t - t_1) \right] \right\} \quad (\text{S.18}) \\ &= \frac{2e}{\hbar} \text{Im} \left\{ \sum_{nm\nu} (-1)^{\nu} \int_{-\infty}^0 dt_1 \int \frac{d\epsilon}{2\pi} e^{-i\epsilon t_1} [\Gamma_s^{\nu}(\epsilon)]_{mn} \left[ G_{nm}^{R\nu}(-t_1) f_s^{\nu}(\epsilon) + G_{nm}^{<\nu}(-t_1) \right] \right\}, \end{aligned}$$

where the linewidth function  $[\Gamma_{\alpha}^{\nu}(\epsilon)]_{mn} = 2\pi \rho_{\alpha}^{\nu}(\epsilon) t_{\alpha,m}^{\nu*}(\epsilon) t_{\alpha,n}^{\nu}(\epsilon)$  in the  $\alpha$  terminal satisfies  $[\Gamma_{\alpha}^{\nu}(\epsilon)]_{nm}^{*} = [\Gamma_{\alpha}^{\nu}(\epsilon)]_{mn}$ , and  $\rho_{\alpha}^{\nu}$  is the density of states. The current is expressed by the Green's function in the region of the junction. It can be written in a more compact form as

$$J_s(t) = \frac{2e}{\hbar} \sum_{\nu} (-1)^{\nu} \int_{-\infty}^0 dt_1 \int \frac{d\epsilon}{2\pi} \text{Im} \left\{ \text{Tr} \left\{ e^{-i\epsilon t_1} \mathbf{\Gamma}_s^{\nu}(\epsilon) \left[ \mathbf{G}_{\nu}^R(-t_1) f_s^{\nu}(\epsilon) + \mathbf{G}_{\nu}^{<}(-t_1) \right] \right\} \right\}, \quad (\text{S.19})$$

where we have changed the superscript  $\nu$  of the Green's function to the subscript. Using  $\text{Tr}[\mathbf{\Gamma}\mathbf{G}]^{*} = \text{Tr}[\mathbf{\Gamma}^{\dagger}\mathbf{G}^{\dagger}]$  we have

$$\begin{aligned} J_s(t) &= \frac{e}{i\hbar} \sum_{\nu} (-1)^{\nu} \int \frac{d\epsilon}{2\pi} \int_{-\infty}^0 dt_1 \left\{ e^{-i\epsilon t_1} f_s^{\nu}(\epsilon) \text{Tr} \left[ \mathbf{\Gamma}_s^{\nu}(\epsilon) \mathbf{G}_{\nu}^R(-t_1) \right] - e^{i\epsilon t_1} f_s^{\nu}(\epsilon) \text{Tr} \left[ \left( \mathbf{\Gamma}_s^{\nu}(\epsilon) \right)^{\dagger} \left( \mathbf{G}_{\nu}^R(-t_1) \right)^{\dagger} \right] \right. \\ &\quad \left. + e^{-i\epsilon t_1} \text{Tr} \left[ \mathbf{\Gamma}_s^{\nu}(\epsilon) \mathbf{G}_{\nu}^{<}(-t_1) \right] - e^{i\epsilon t_1} \text{Tr} \left[ \left( \mathbf{\Gamma}_s^{\nu}(\epsilon) \right)^{\dagger} \left( \mathbf{G}_{\nu}^{<}(-t_1) \right)^{\dagger} \right] \right\} \quad (\text{S.20}) \\ &= \frac{e}{i\hbar} \sum_{\nu} (-1)^{\nu} \int \frac{d\epsilon}{2\pi} \text{Tr} \left\{ \mathbf{\Gamma}_s^{\nu}(\epsilon) \left( \mathbf{G}_{\nu}^{<}(\epsilon) + f_s^{\nu}(\epsilon) \left[ \mathbf{G}_{\nu}^R(\epsilon) - \mathbf{G}_{\nu}^A(\epsilon) \right] \right) \right\}. \end{aligned}$$

The lesser Green's function can be solved by the Keldysh equation

$$\mathbf{G}_{\nu}^{<}(\epsilon) = \sum_{\mu} \mathbf{G}_{\nu\mu}^R(\epsilon) \mathbf{\Sigma}_{\mu}^{<}(\epsilon) \mathbf{G}_{\mu\nu}^A(\epsilon), \quad (\text{S.21})$$

where the self-energy

$$\Sigma_{nm}^{<\mu\mu}(\epsilon) = \sum_{p\alpha=l,s} t_{p\alpha,n}^{\mu*} g_{p\alpha}^{<\mu}(\epsilon) t_{p\alpha,m}^{\mu} \quad (\text{S.22})$$

is due to the coupling with the electrode and the STM tip, which is diagonal in the Nambu space. Using Eq. (S.16) we have

$$\begin{aligned} g_{p\alpha}^{<\nu}(\epsilon) &= \int dt e^{i\epsilon t} g_{p\alpha}^{<\nu}(t) = 2\pi i f_{\alpha}^{\nu}(\epsilon_{p\alpha}^{\nu}) \delta(\epsilon - \epsilon_{p\alpha}^{\nu}), \\ g_{p\alpha}^{R,A\nu}(\epsilon) &= \int dt e^{i\epsilon t} g_{p\alpha}^{R,A\nu}(t) = \frac{1}{\epsilon - \epsilon_{p\alpha}^{\nu} \pm i0^{+}}, \end{aligned} \quad (\text{S.23})$$

which yields

$$\begin{aligned} \Sigma_{nm}^{<\nu\nu}(\epsilon) &= i[(\Gamma_s^{\nu})_{nm} f_s^{\nu}(\epsilon) + (\Gamma_l^{\nu})_{nm} f_l^{\nu}(\epsilon)], \\ \Sigma_{nm}^{R,A\nu\nu}(\epsilon) &= \mp \frac{i}{2}[(\Gamma_s^{\nu})_{nm} + (\Gamma_l^{\nu})_{nm}], \end{aligned} \quad (\text{S.24})$$

or formally,

$$\begin{aligned}\Sigma_\nu^<(\epsilon) &= i[\Gamma_s^\nu(\epsilon)f_s^\nu(\epsilon) + \Gamma_l^\nu(\epsilon)f_l^\nu(\epsilon)], \\ \Sigma_\nu^{R,A}(\epsilon) &= \mp \frac{i}{2}[\Gamma_s^\nu(\epsilon) + \Gamma_l^\nu(\epsilon)].\end{aligned}\quad (\text{S.25})$$

Applying the Dyson equation

$$[\mathbf{G}^{R,A}]^{-1} = [\mathbf{g}^{R,A}]^{-1} - \Sigma^{R,A}, \quad (\text{S.26})$$

we have

$$[\mathbf{G}^A]^{-1} - [\mathbf{G}^R]^{-1} = \Sigma^R - \Sigma^A, \quad (\text{S.27})$$

and then

$$\mathbf{G}^R(\epsilon) - \mathbf{G}^A(\epsilon) = \mathbf{G}^R(\epsilon)[\Sigma^R(\epsilon) - \Sigma^A(\epsilon)]\mathbf{G}^A(\epsilon). \quad (\text{S.28})$$

The diagonal elements are

$$\mathbf{G}_\nu^R(\epsilon) - \mathbf{G}_\nu^A(\epsilon) = \sum_\mu -i\mathbf{G}_{\nu\mu}^R(\epsilon)[\Gamma_l^\mu(\epsilon) + \Gamma_s^\mu(\epsilon)]\mathbf{G}_{\mu\nu}^A(\epsilon). \quad (\text{S.29})$$

Inserting the lesser self-energy  $\Sigma^<$  and the relation above into Eq. (S.20) yields

$$\begin{aligned}J_s &= \frac{e}{h} \sum_{\nu\mu} (-1)^\nu \int \frac{d\epsilon}{2\pi} \text{Tr} \left\{ \Gamma_s^\nu(\epsilon) \left( \mathbf{G}_{\nu\mu}^R(\epsilon) [\Gamma_s^\mu(\epsilon)f_s^\mu(\epsilon) + \Gamma_l^\mu(\epsilon)f_l^\mu(\epsilon)] \mathbf{G}_{\mu\nu}^A(\epsilon) - f_s^\nu(\epsilon) \mathbf{G}_{\nu\mu}^R(\epsilon) [\Gamma_s^\mu(\epsilon) + \Gamma_l^\mu(\epsilon)] \mathbf{G}_{\mu\nu}^A(\epsilon) \right) \right\} \\ &= \frac{e}{h} \sum_\nu (-1)^\nu \int d\epsilon \text{Tr} \left\{ (f_s^\nu - f_s^\nu) \Gamma_s^\nu \mathbf{G}_{\nu\nu}^R \Gamma_s^\nu \mathbf{G}_{\nu\nu}^A + (f_l^\nu - f_s^\nu) \Gamma_s^\nu \mathbf{G}_{\nu\nu}^R \Gamma_l^\nu \mathbf{G}_{\nu\nu}^A + (f_l^\nu - f_s^\nu) \Gamma_s^\nu \mathbf{G}_{\nu\nu}^R \Gamma_l^\nu \mathbf{G}_{\nu\nu}^A \right\}.\end{aligned}\quad (\text{S.30})$$

Assume that the local electrode is biased with the STM tip and the superconductor with energy  $eV$ , the zero-temperature differential conductance  $\sigma(eV) = \partial J_s / \partial V$  is given by

$$\sigma = \frac{e^2}{h} \sum_{a,b} \zeta_{ab} \text{Tr} [\Gamma_s^a \mathbf{G}_{ab}^R \Gamma_l^b \mathbf{G}_{ba}^A], \quad (\text{S.31})$$

where  $\zeta_{ab} = -1$  if  $a, b$  are both electron/hole states; otherwise,  $\zeta_{ab} = 1$ .

In the present system, the tunneling Hamiltonian is

$$H_T = \sum_{p,\alpha=l,s} t_\alpha c_{p\alpha}^\dagger \Psi(\mathbf{x}_\alpha) + h.c., \quad (\text{S.32})$$

and the corresponding linewidth function is

$$\Gamma_\alpha^a(\mathbf{x}_1, \mathbf{x}_2, E) = 2\pi \rho_\alpha^a |t_\alpha|^2 \delta(\mathbf{x}_1 - \mathbf{x}_\alpha) \delta(\mathbf{x}_2 - \mathbf{x}_\alpha), \quad (\text{S.33})$$

with  $\mathbf{x}_{l(s)}$  the location of local electrode (STM tip). Under the tunneling limit in our setup, the multiple tunneling has negligible contribution to the nonlocal current. Then we can insert Eq. (S.9) into the conductance formula (S.31) and obtain

$$\begin{aligned}\sigma(eV) &= \frac{e^2}{h} \sum_{a,b} \zeta_{ab} \int d\mathbf{x}_1 d\mathbf{x}_2 d\mathbf{x}_3 d\mathbf{x}_4 \Gamma_l^a(\mathbf{x}_1, \mathbf{x}_2, E) \mathbf{G}_{ab}^R(\mathbf{x}_2, \mathbf{x}_3, E) \Gamma_s^b(\mathbf{x}_3, \mathbf{x}_4, E) \mathbf{G}_{ba}^A(\mathbf{x}_4, \mathbf{x}_1, E) \\ &= \frac{e^2}{h} \sum_{a,b} \zeta_{ab} |2\pi t_l t_s|^2 \rho_l \rho_s \mathbf{G}_{ab}^R(\mathbf{x}_l, \mathbf{x}_s, E) \mathbf{G}_{ba}^A(\mathbf{x}_s, \mathbf{x}_l, E) \\ &= \sigma_0(eV) \sum_{a,b} \zeta_{ab} \left| \int dk_y dk_z \frac{1}{4\pi^2} \frac{\rho_{k_y, k_z}}{\rho_N} r_{ba}^0 e^{i[k_y(y'-y) + k_z(z'-z)]} e^{-i[k_a x + k_b x']} \right|^2.\end{aligned}\quad (\text{S.34})$$

with  $\sigma_0(eV) = (e^2/h) |2\pi t_l t_s \rho_N|^2 \rho_l \rho_s$  and  $\rho_N$  is the density of states in nodal line semimetal.

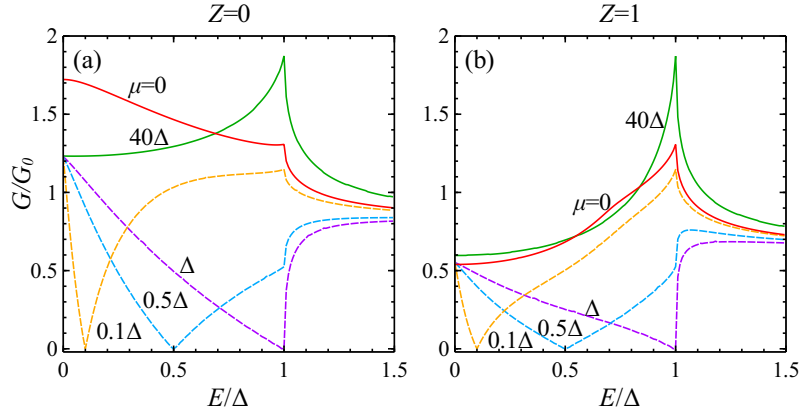


FIG. S.2. Conductance spectra for (a) zero and (b) finite interface barrier with different chemical potentials. All relevant parameters are the same as those in Fig. 3 in the main text.

### Tunneling conductance of the junction

In this section, we calculate the longitudinal conductance across the junction. Inserting the reflection coefficients into the Blonder-Tinkham-Klapwijk formula [2] yields

$$G(eV) = \frac{e^2 S}{4\pi^2 \hbar} \int dk_y dk_z \left[ 2 + \sum_{i,j=1,2} (A_{ji} - B_{ji}) \right], \quad (\text{S.35})$$

where  $S$  is the cross-section area of the junction. The numerical results of the reduced conductance  $G/G_0$  are shown in Fig. S.2, where  $G_0(eV) = G(eV)|_{A_{ji}=B_{ji}=0}$  is the conductance of the uniform nanowire along the  $x$  direction. For zero interface barrier in Fig. S.2(a), the conductance spectra resemble those of graphene [8] but with a different physical meaning. Here, an AAR-to-RAR crossover takes place as the chemical potential increases, which is different from the SAR-to-RAR transition in graphene. Moreover, for a finite interface barrier in Fig. S.2(b), even the conductance spectra of AAR and RAR become similar and cannot be discriminated. We conclude that different types of AR cannot be identified by the tunneling conductance spectra.